# Single-Neuron Modeling of LSO Unit Responses

MIRIAM ZACKSENHOUSE,[1] DON H. JOHNSON,[1] JEROME WILLIAMS,[1] AND CHIYEKO TSUCHITANI[2]
[1]*Department of Electrical and Computer Engineering, Rice University, Houston 77005-1892; and* [2]*Department of Neurobiology and Anatomy Medical School, The University of Texas Health Science Center, Houston, Texas 77030-1825*

**Zacksenhouse, Miriam, Don H. Johnson, Jerome Williams, and Chiyeko Tsuchitani.** Single-neuron modeling of LSO unit responses. *J. Neurophysiol.* 79: 3098–3110, 1998. We investigated, using a computational model, the biophysical correlates of measured discharge patterns of lateral superior olive (LSO) neuron responses to monaural and binaural stimuli. The model's geometry was based on morphological data, and static electric properties of the model agree with available intracellular responses to hyperpolarizing current pulses. Inhibitory synapses were located on the soma and excitatory ones on the dendrites, which were modeled as passive cables. The active properties of the model were adjusted to agree with statistical measures derived from extracellular recordings. Calcium-dependent potassium channels supplemented the usual Hodgkin-Huxley characterization for the soma to produce observed serial interspike interval dependence characteristics. Intracellular calcium concentration is controlled by voltage- and calcium-dependent potassium channels and by calcium diffusion and homeostatic mechanisms. By adjusting the density of the calcium-dependent potassium channels, we could span the observed range of transient response patterns found in different LSO neurons. Inputs from the two ears were modeled as Poisson processes to describe the responses to tone-burst stimuli. Transient and sustained responses to monaural and binaural tone-burst stimuli over a wide range of stimulus conditions could be well described by varying only the model's inputs. As found in recordings, model responses having similar discharge rates but different binaural stimulus combinations exhibited differences in interval statistics.

## INTRODUCTION

The lateral superior olive (LSO) is the first nucleus in the ascending auditory pathway involved in the binaural processing of mid- to high-frequency (>1 kHz) sounds. Binaural processing in the LSO involves excitatory/inhibitory interactions: LSO neurons are excited by stimulation of the ipsilateral ear and inhibited by stimulation of the contralateral ear (E/I neurons) (Boudreau and Tsuchitani 1968; Goldberg and Brown 1969; Guinan et al. 1972). The ipsilateral excitatory projections to the LSO are believed to arise from the spherical/bushy cells in the anteroventral cochlea nucleus (AVCN) and to end on the distal dendrites of LSO cells (Cant 1984; Cant and Casseday 1986; Glendenning et al. 1985). The AVCN spherical/bushy cells almost exclusively produce primary-like (similar to auditory-nerve fibers) tone-burst discharge patterns (Bourk 1976). LSO input from the contralateral ear arises from the principal/globular cells of the medial nucleus of the trapezoid body (MNTB), which receives contralateral inputs from the AVCN globular/bushy cells (Cant 1991). The projections from the MNTB principal cells end on the soma and the proximal dendrites of LSO principal cells with terminals believed to be inhibitory (Cant 1984). The MNTB principal cells produce tone-burst responses that are primary-like or pri-notch type (primary-like, but with a short 1- to 2-ms period of spike suppression after the 1st spike) (Guinan et al. 1972). Intracellular measurements of excitatory postsynaptic potentials (EPSPs) and inhibitory postsynaptic potentials (IPSPs) in LSO slices taken from gerbil suggest that ~10 excitatory neurons converge on the dendritic tree and ~8 inhibitory ones on the soma of a single LSO neuron (Sanes 1990).

The excitatory/inhibitory interactions occurring in each LSO neuron are not symmetrically opposite: the statistical characteristics of the discharges elicited under different ipsilateral and contralateral stimulus conditions are clearly distinguishable even when the mean discharge rate is maintained (Tsuchitani 1988a). Point process analysis suggests that the inhibition is mainly a shunting (divisive) effect (Zacksenhouse et al. 1992). This, along with morphological (Cant and Casseday 1986; Glendenning et al. 1985) and pharmacological (Moore and Caspary 1983; Wenthold et al. 1987) evidence suggests that chloride channels located on the soma and proximal dendrites mediate inhibition in LSO neurons.

Initial discharges in LSO tone-burst responses are tightly time locked to stimulus onset and produce peaks in the post-stimulus-onset time (PST) histogram (Boudreau and Tsuchitani 1970; Pfeiffer 1966; Tsuchitani 1982, 1988b). This characteristic initial response pattern, commonly termed the chopping response, is transient: initial peaks in the PST histogram become wider and are eventually obscured in the sustained response (Fig. 1, *left column*). The initial discharge rates (over the 1st 40 ms after stimulus onset) in response to specific stimuli (monaural tone bursts at the unit's characteristic frequency and at stimulus levels between 25 and 35 dB) are used to classify the LSO units into two broad categories (Tsuchitani and Johnson 1985), which are also distinguished based on the characteristics of the chopping and sustained response. Slow choppers responded with initial rates lower than 400 spikes/s and generated chopping pattern characterized by one to three narrow peaks followed by broad and widely spaced peaks (Fig. 1, *left top panel*). The sustained discharges of slow choppers are characterized by low rates (<300 spikes/s), relatively symmetric interval histograms (skew < 0.3), and gradually increasing recovery functions (Fig. 1, *middle top panel*). Fast choppers responded with initial rates higher than 400 spikes/s and generated chopping patterns characterized by multiple narrow and closely spaced peaks (Fig. 1, *left middle panel*). The sustained discharges of fast choppers are characterized by higher rates, asymmetric interval histograms, and recov-

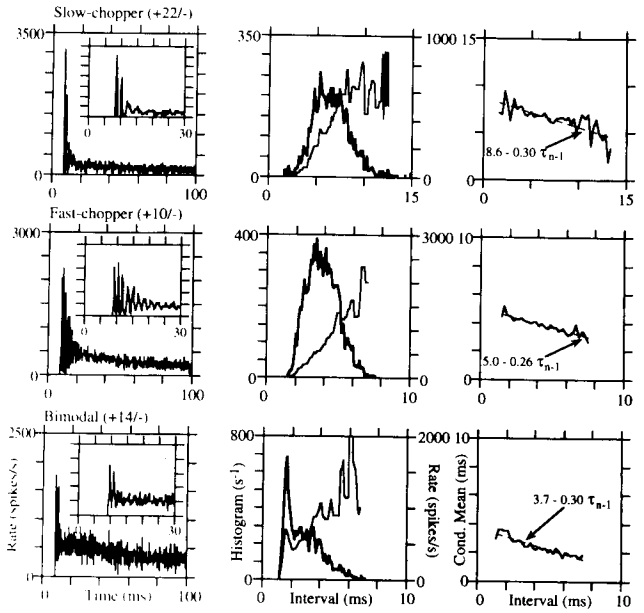


FIG. 1. Characteristics of measured lateral superior olive (LSO) tone-burst responses. Poststimulus-onset time (PST) histograms (*left column*) interval histograms (*middle column,* bold), recovery functions (*middle column,* thin), and conditional mean functions (*right column*) of a slow chopper [*top row;* slow chopper B in Zacksenhouse et al. (1995)], a fast chopper [*middle row;* fast chopper B in Zacksenhouse et al. (1995)], and a bimodal unit (*bottom row*) in response to tone bursts at each neuron's characteristic frequency. See METHODS and Johnson (1996) for definitions and properties of these response measures. Binaural stimulus levels expressed in dB above unit threshold with the convention (ipsilateral level/contralateral level) are indicated above the *top left corner* of the PST histograms. A contralateral level indicated by a dash means that no contralateral stimulus was presented, which means that the monaural response is shown. Each PST histogram panel contains a high-resolution PST histogram that better displays the chopping response found in the 1st 30 ms. A linear fit is superimposed on the conditional mean functions and is specified by the indicated equation. The binwidths of all PST histograms are 250 $\mu$s. The binwidths of the interval statistics are (from top to bottom) 150, 100, and 100 $\mu$s.

ery functions that may exhibit the rebound effect [a step change immediately after the deadtime (Zacksenhouse et al. 1992)] (Fig. 1, *middle panel* presents analysis of discharges elicited by slowly driven fast chopper that exhibits the rebound effect when driven to higher rates, as shown in Fig. 14, *top right*). Although most units produce unimodal interval histograms, some produce bimodal interval histograms and are therefore classified separately as bimodal units (Fig. 1, *bottom row*). Bimodal-unit recovery functions may include a negatively aging section, during which postspike firing rate decreases momentarily with the time since the last spike.

All LSO neurons, regardless of unit type, produce spike trains that exhibit first-order negative interspike interval serial dependence (Tsuchitani and Johnson 1985), as evident in the negatively sloped conditional mean estimates (Fig. 1, *right column*): long intervals tend to follow short ones and vice versa. The strength of the serial dependence, as estimated by the slope of the conditional mean, seems to be independent of the stimulus conditions. Theoreticians have predicted that the observed negative serial dependence results from a cumulative afterhyperpolarization (CAHP) effect mediated by calcium-dependent potassium channels (Smith and Goldberg 1986; Zacksenhouse et al. 1992).

Modeling studies show that the magnitude and extent of an LSO unit's transient chopping response does not result solely from the neuron's dead time or from the transient in the primary-like inputs to the LSO (Zacksenhouse 1993; Zacksenhouse et al. 1995). We hypothesized that the spike generation process itself undergoes a change during the onset of the tone-burst response, possibly due to transients in calcium concentration. Thus calcium may mediate two aspects of LSO response patterns: serial dependence of interspike intervals and the characteristic transient chopping response.

Previous LSO modeling efforts have focused on azimuthal processing encoding in the average rate response's statistical properties (Blum and Reed 1991; Colburn and Moss 1981; Dabak and Johnson 1992; Reed and Blum 1990). Temporal and statistical aspects of spike trains produced by LSO neurons in response to tone-burst stimuli are fully characterized (during both the chopping response and the sustained response) by a specific point process model (Zacksenhouse et al. 1992, 1993, 1995). The point process model characterizes the discharge patterns by describing the underlying recovery function. The recovery function describes how the cell recovers from spike generation in terms of the postspike discharge rate. By proper selection of model parameters, which can be estimated directly from measured discharges, the model accurately approximates the tone-burst responses of all LSO unit types. We expected that a single biophysical model of LSO neurons could describe different unit types and can serve to provide insight into the biophysical correlates of the different LSO unit types.

The recovery function, so important in mathematical models, also constrains the biophysical mechanisms that may be involved in spike generation and information processing. Another set of recently available constraints come from intracellular recording made in vitro from LSO neurons in the mouse (Wu and Kelly 1991) and in the gerbil (Sanes 1990). We undertook the biophysical modeling work to determine whether such constraints, derived from extracellular and intracellular recordings, are consistent and sufficient: can the type of biophysical mechanisms and the corresponding values of their parameters be determined to yield a model that accurately reproduces the observed response?

## METHODS

### *Computational model*

We primarily used the NEURON (developed by Michael Hines at Yale) general purpose neuron simulators. We have developed simulations of LSO neurons with both the NEURON and GENESIS simulation environments; initial results derived using GENESIS and NEURON have been presented elsewhere (Johnson et al. 1994a,b).

A prototype model for LSO neurons was established based on the anatomic and intracellular data. The LSO neuron is represented as a cylindrical soma, two cylindrical dendritic branches connected at its ends, and a short axonal cylinder connected at the center (Fig. 2). This geometry reflects the bipolar shape of LSO neurons (Cant 1984). The membrane of the model's dendritic compartments is passive. The kinetics of the active membrane in the somatic and axonal compartments of the prototype are based on a variant of Hodgkin-Huxley model (Hodgkin and Huxley 1952) used by Banks and Sachs in their model of chopper units in the AVCN (Banks and Sachs 1991). New channels were added to the

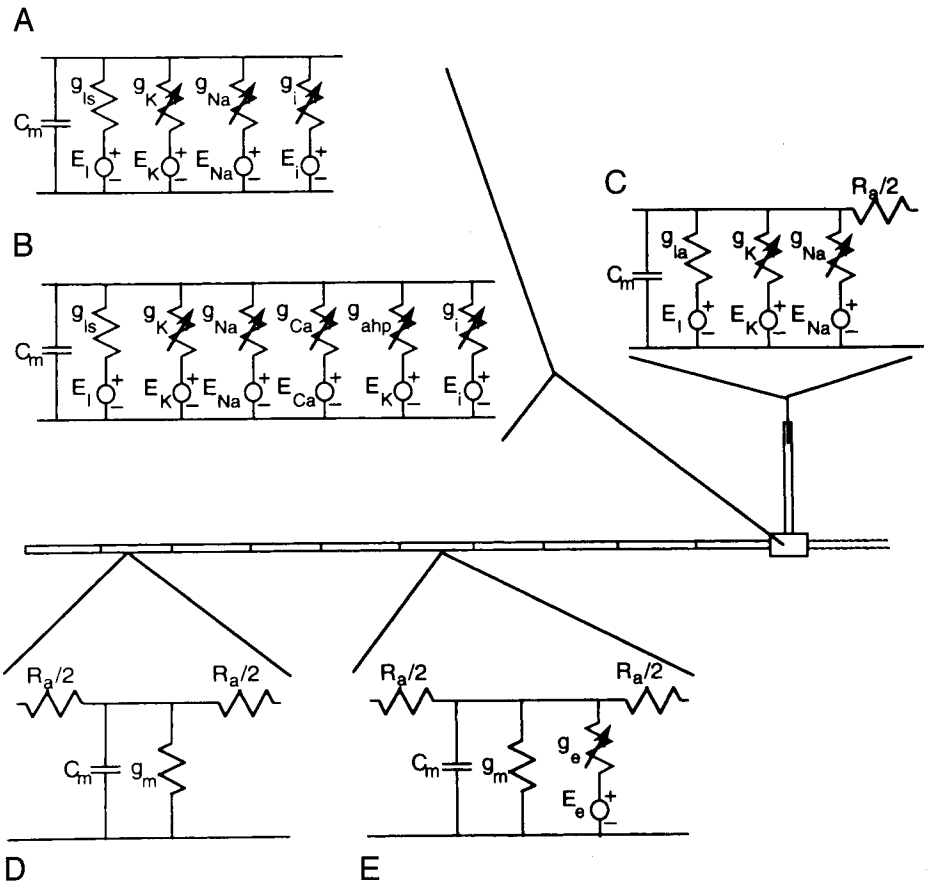


FIG. 2. Illustration of the compartmental model. The model includes 2 dendritic cylinders emanating from a somatic compartment. Each dendritic cylinder is divided into 10 isopotential compartments connected by axial resistors. The equivalent circuit of the somatic (*a*, prototype; *b*, final), axonal (*c*), and dendritic (*d*, without; *e*, with excitatory inputs) compartments are illustrated. Excitatory synapses are placed at the 5th compartments along each dendritic cylinder as shown. Additional excitatory synapses are added and placed closer to the soma as needed (not shown). Inhibitory synapses are placed at the soma. The equations underlying the model are described in the APPENDIX, and parameter values are specified in Table 1.

prototype only after assuring that the observed response properties cannot be produced by parameter variations. Single neuron responses to different stimulus conditions have been simulated by changing or augmenting input innervation only. Finally, the different response types elicited by different neurons have been simulated with parsimonious parameter variations. The equations underlying the model are given in the APPENDIX.

INPUT CHARACTERISTICS AND INNERVATION. To match with known anatomy and physiology, we placed the ipsilateral, excitatory inputs to the model LSO neurons on the dendrites and the contralateral, inhibitory inputs on the soma (Fig. 2). We placed excitatory synapses at the middle of each dendritic branch and added additional synapses located closer to the soma as necessary to simulate the effect of increasing excitatory stimulus level. Excitatory synapses had a reversal potential of 0 mV, whereas inhibitory synapses had a reversal potential of −75 mV [based on in vitro measurements from Sanes (1990)]. The time constants for the excitatory and inhibitory synapses were selected so that the duration of the resulting EPSPs and IPSPs at the somatic compartment of the model would agree with intracellular recordings (Sanes 1990). In particular, these recordings demonstrated that EPSPs are consistently narrower than IPSPs. However, because the excitatory synapses are located further away from the soma, their EPSPs are filtered and smoothed by the dendritic compartments. Thus to produce the recorded relationship between the durations of EPSPs and IPSPs, despite their relative locations, the time constant of the inhibitory synapses have to be much longer (5-fold) than the time constant of the excitatory synapse. The long time constant of the inhibitory synapses is critical in producing the shunting effect of inhibition that was postulated based on point process analysis (Zacksenhouse et al. 1992). Each synaptic event is described by an alpha function conductance change with maximum conductance change $\bar{g}$ and time constant $\tau$ (the alpha wave reaches its maximum conductance $\bar{g}$ at time $\tau$). Different parameter values were chosen for excitatory and inhibitory conductance changes (see Table 1 for details). Each input was assumed to be a primary-like discharge pattern, which is well modeled by a dead time–modified Poisson process with an exponentially decaying rate. Because several inputs converge on a single LSO neuron, the total input is given by a superposition of the individual inputs and is well approximated by a single Poisson process (with no dead time). This approximation, however, does not capture the possible synchronization of the initial spikes at stimulus onset. Nevertheless, the inputs, both excitatory and inhibitory, are modeled here as inhomogeneous (nonstationary) Poisson processes. The rate $\lambda(t)$ of the input process describes a short-term adaptation and a steady-state rate typical of primary-like tone-burst responses

$$\lambda(t) = A_{tr} \exp\{-t/\tau_{tr}\} + A_{ss}$$

Here, $\tau_{tr}$, the time constant of the transient term, is 18 ms, and $A_{ss}$ and $A_{tr}$ vary with stimulus level. We selected the amplitude of the steady-state rate $A_{ss}$ to produce the desired output rate and the amplitude of the transient driven rate $A_{tr}$ to evoke the desired chopping response. The inputs to each synaptic location were generated independently off-line and stored as input files. Each input file includes 100 different realizations of the same inhomogeneous Poisson process, with each realization lasting 100 ms and separated by 45 ms of silence (0 input).

DENDRITIC MODEL. Each dendritic cylinder represents the collapsed dendritic tree emanating from each pole of the LSO cell body. We assumed that the electrotonic length $L$, the length expressed in terms of the space constant, of each dendritic branch is unity ($L = 1.0$). Each dendritic cylinder is divided into 10 isopotential passive compartments connected by an axial resistivity $R_a$.

TABLE 1. *Parameters used in the final compartmental model of LSO neurons*

| Parameter | Value |
|---|---|
| Number of dendrites | 2 |
| Dendrite membrane resistance $R_m$ | 3,000 Ω/cm$^2$ (1,500–3,000 Ω/cm$^2$) |
| Dendrite membrane capacitance $C_m$ | 1 μF/cm$^2$ |
| Axial resistance $R_a$ | 150 Ω/cm |
| Dendritic diameter | 3.4 μm (3.4–4.3 μm) |
| Dendrite electronic length $L$ | 1.0 |
| Soma diameter | 11 μm |
| Soma length | 23 μm |
| Axon diameter | 3 μm |
| Axon length | 70 μm |
| Resting potential $V_{init}$ | −62 mV |
| Sodium reversal potential $E_{Na}$ | 55 mV |
| Potassium reversal potential $E_K$ | −80 mV |
| Excitatory synapse | |
| Reversal potential $E_{exc}$ | 0 mV |
| Maximum conductance $\bar{g}_{exc}$ | 7.5 μS |
| Time constant $\tau_{exc}$ | 0.2 ms |
| Inhibitory synapse | |
| Reversal potential $E_{inh}$ | −75 mV |
| Maximum conductance $\bar{g}_{inh}$ | 3.0 μS |
| Time constant $\tau_{inh}$ | 1 ms |
| Axon leakage conductance $g_{la}$ | 25 μS/cm$^2$ |
| $\bar{g}_{Na}$ (axon) | 0.17 S/cm$^2$ |
| $\bar{g}_K$ (axon) | 20 mS/cm$^2$ |
| Soma leakage conductance $g_{ls}$ | 90 μS/cm$^2$ |
| $\bar{g}_{Na}$ (soma) | 0.17 S/cm$^2$ |
| $\bar{g}_K$ (soma) | 40 mS/cm$^2$ |
| $\bar{g}_{Ca}$ (soma) | 3.5 mS/cm$^2$ |
| $\bar{g}_{AHP}$ (soma) | 26 mS/cm$^2$ (15–35 mS/cm$^2$) |
| $\delta_0$ | 0.8 |
| depth of outer shell $d$ | 320 Å |
| Pump time constant $\tau_p$ | 17.5 ms |
| Pump equilibrium concentration $\chi_0$ | $5 \times 10^{-5}$ mM |
| Calcium concentration outside the cell | 4 mM |

Example outputs from those shown in Figs. 4 and 7–14. The reference set of parameters is listed with the range of those parameters that have been varied in other simulations in parentheses. LSO, lateral superior olive.

Each isopotential compartment is modeled as an equivalent circuit with a leakage branch (membrane resistance $R_m$), in parallel with a capacitive branch (membrane capacitance $C_m$). An excitatory synaptic branch, modeled by a time-varying conductance, is added in parallel with those compartments receiving excitatory inputs (Fig. 2).

Given the large surface area of the dendritic branches, their electrical properties dominate the cell's static response to hyperpolarizing current pulses. Such responses can be characterized by the membrane input resistance and the membrane time constant. Intracellular measurements are not available from LSO neurons in the cat, so we rely on measurements made in vitro from LSO neurons of the mouse and the gerbil. In the mouse, the membrane input resistance was measured to be 30 ± 16 (SD) MΩ with time constant of 2.96 ± 0.84 ms (Wu and Kelly 1991). In the gerbil, the membrane input resistance was measured to be 42 ± 21 MΩ with time constant of 1.1 ± 0.4 ms (Sanes 1990). Although the membrane resistance of LSO neurons in both the mouse and the gerbil are similar, the membrane time constants are not. We developed the models to exhibit a membrane time constant of 2–4 ms.

If we assume a default value for the membrane capacitance $C_m$ = 1.0 μF/cm$^2$ (Hille 1992), the dendritic membrane resistance $R_m$ can be determined to result in the desired time constant (with $\tau_m = R_m C_m$). The membrane input resistance of a single cylinder $R_{input} = (R_m R_a / 2r^3)^{1/2}[\coth(L)/\pi]$ (Rall 1989) can then be used to determine the radius of the dendritic cylinder (given $L$ = 1.0 and assuming a standard value for the axial resistivity $R_a$ = 150 Ω/cm). We have tested the above selection of passive parameters by simulating the response of the model to hyperpolarizing current injection. The simulated responses agree, both in magnitude and in time constant, with those measured in vitro, as reported in Fig. 2 of Wu and Kelly (1991).

SOMATIC AND AXONAL MODEL. We modeled the soma as an isopotential cylindrical compartment with dimensions based on anatomic drawings of Golgi-impregnated cat LSO neurons (Cant 1984). A single axonal compartment is connected to the middle of the somatic compartment. The prototype model of the somatic and axonal membrane's active properties incorporates only the voltage-dependent $Na^+$ and $K^+$ channels and the leakage channels detailed in the APPENDIX.

On the basis of the hypothesized biophysical origin of serial dependence (Zacksenhouse et al. 1992), we added mechanisms to affect the concentration of calcium in the somatic compartment and calcium-dependent potassium channels to affect the afterhyperpolarization (AHP) of the somatic membrane potential accordingly (Fig. 2). (These potassium channels are referred to as the AHP channels. The AHP channels and the calcium mechanisms are inserted only in the somatic compartment.) The conductance of the calcium-dependent potassium channels $g_{AHP}$ is governed by an activator state variable $q$, whose dynamics depend on calcium concentration $\chi$ in a submembrane shell of depth $d$ = 315 Å. The submembrane calcium concentration $\chi$ increases with inward influx of $Ca^{2+}$ through calcium channels and decreases by a first-order process with a time constant $\tau_p$. This last process simulates both the outward pumping of calcium and the diffusion of calcium toward the center of the cell. The conductance of the calcium channels $g_{Ca}$ is governed by an activation state variable $s$, whose dynamics depend on the membrane potential, and by an inactivation state variable $r$, whose dynamics depend on $\chi$. This approach to the modeling of calcium mechanisms is similar to the one pursued by Traub for simulating intrinsic bursting in CA3 hippocampal neurons (Traub 1982; Traub et al. 1991). However, we modified the kinetics of these channels by shifting the steady-state curves of the above state variables and by scaling the time constant curve of their rate of change. The most significant effect of these changes is that the slow calcium-mediated spikes that give rise to the bursting activity in CA3 hippocampal neurons do not occur in our model (see the APPENDIX).

Because of the large changes in submembrane calcium concentration $\chi$, it is necessary to update the calcium reversal potential $E_{Ca}$ with time as a function of $\chi$. The initial calcium concentration $\chi$ is set to null the net change in calcium concentration at resting potential. The reversal potential of the leakage battery is set automatically by NEURON to null the total current through the membrane of the somatic compartment at rest.

## *Statistical measures*

We analyzed simulated discharges using standard statistical measures that have been applied to neural responses (Johnson 1978, 1996; Johnson et al. 1986; Snyder 1975). Briefly, the PST histogram is computed from multiple (here 100) spike trains produced by a single instance of the model (defined by its parameters) responding to different realizations of the same input processes. The number of spikes occurring at the same bin at a given time after the stimulus onset are normalized by the binwidth to describe the poststimulus discharge rate.

The interval histogram INT($l$) is computed by normalizing the relative number of interspike intervals that lie in bin $l$ by the binwidth $\delta$. The recovery function REC($l$) is computed from the interval histogram by

$$\mathrm{REC}(l) = \frac{\mathrm{INT}(l)}{\sum_{k=l}^{l_{\max}} \mathrm{INT}(k)\delta}$$

and describes the postspike discharge rate. Clearly, this computation of the recovery function becomes unreliable at the tail of the interval histogram, as the numerator and denominator become small and are based on small number of intervals (Johnson 1996). This limitation directs how we evaluate and compare recovery functions: fluctuations and differences at long intervals that fall at the tail of the interval histogram (defined to be 5% of the total number of available intervals) are discounted.

The conditional mean is computed by grouping the interspike intervals according to the duration of their previous intervals, and then computing the average duration of each group separately. The characteristics of the computed conditional mean function are most reliable at the mode(s) of the interval histogram and are less reliable at short and long intervals where the corresponding groups contain fewer discharges (Johnson 1996). The conditional mean provides a measure of the first-order serial dependence between successive interspike intervals. Independent interspike intervals give rise to flat conditional mean functions because the duration of an interval is not affected by the duration of the previous interval. Conditional mean functions and interval histograms are computed from the sustained portion of the response (occurring later than 40 ms from response onset as measured by the PST histogram).

### *Recordings*

We recorded extracellularly from single units in the LSO of adult cats anesthetized with pentobarbital sodium; recording details are described elsewhere (Tsuchitani 1988b; Tsuchitani and Johnson 1985). Tone bursts, set to the excitatory characteristic frequency, were presented monaurally to the ear ipsilateral to the recording site, or binaurally to both ears. The responses analyzed here have also been studied in previous reports (Zacksenhouse et al. 1992, 1993, 1995).

## RESULTS

### *Prototype model does not produce serial dependence*

Spike trains elicited by the prototype model described above (with only voltage-dependent $Na^+$ and $K^+$ channels in the somatic membrane) exhibit flat conditional mean plots (Fig. 3, *bottom right*), suggesting that the duration of an interspike interval has no effect on the average duration of the next interval. In contrast, spike trains elicited by LSO neurons exhibit negative serial dependence between successive intervals and negatively sloped conditional mean functions. The tone-burst response elicited by the prototype does exhibit a transient chopping response at stimulus onset, as evident in the PST histogram in the *top right panel* of Fig. 3. However, the peaks are too wide and too widely spaced, and the initial two peaks are not closely spaced, as compared with transient chopping response characteristic of LSO neurons. Although the sustained response is typical of LSO neurons, the amplitude of the chopping peaks are not as high as those produced by LSO neurons, despite the high transient-to-sustained discharge rate ratio of the input process (Fig. 3, *top left;* Table 2). The amplitude of the peaks could be increased by increasing the transient input rate, but the width and spacing of the peaks would not be affected because, in the absence of serial correlation, they are determined mainly by interspike interval distribution. These simulations consistently produced responses that did not agree with those recorded from the LSO.

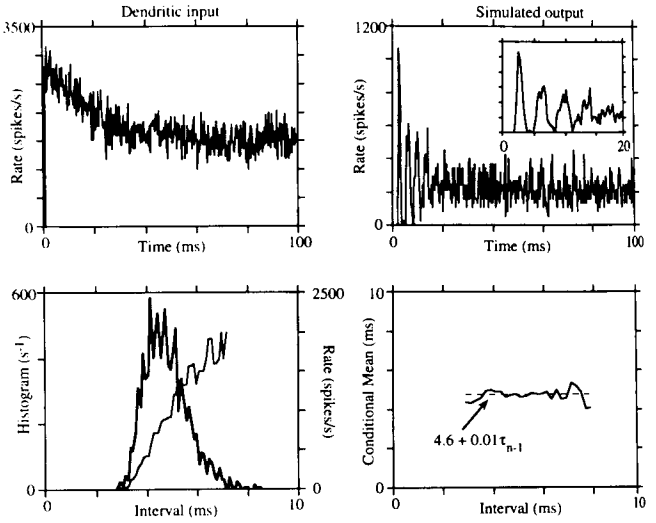


FIG. 3. Prototype model response characteristics: no serial dependence. The prototype model (no calcium mechanisms, Fig. 2) with the reference set of parameters (except for the maximum excitatory conductance $\bar{g}_{exc}$, which equals 2.5 $\mu S/cm^2$) is excited by spike trains produced by an inhomogeneous Poisson process ($A_{ss} = A_{tr}$ = 1,500 spikes/s). The PST histograms of the input and output spike trains are shown in the *top panels* (binwidth 250 $\mu$s). The chopping response of the prototype model does not resemble the chopping response of LSO neurons (see Fig. 1 and text). The interval histogram and recovery function are shown at the *bottom left panel* (bold and thin lines, respectively, binwidth 100 $\mu$s). The best linear fit is superimposed on the conditional mean function (*bottom right,* binwidth 200 $\mu$s), which demonstrates a lack of serial dependence.

### *AHP channels give rise to serial dependence*

Calcium-dependent potassium channels inserted in the somatic membrane, along with calcium channels and the calcium pump, can affect the serial dependence between successive interspike intervals. Spike trains elicited by this model exhibit the characteristic negative serial dependence between successive interspike intervals, as evident from the negatively sloped conditional mean function in Fig. 4. The resulting PST histogram (Fig. 4, *top right*) exhibits a transient chopping response similar to those produced by LSO unit discharges, even though the transient to sustained discharge rate ratio of the input process is low (Fig. 4, *top left;* compare with the input used to drive the prototype model, Fig. 3, *top left*). Producing a better match of sustained response characteristics would have sacrificed agreement with the chopping response. The spike trains produced by the final model in response to depolarizing current injection resemble those recorded in vitro (Wu and Kelly 1991, Fig. 2). Note the effect of the AHP channels on the shape of the interspike interval histogram (Figs. 3 and 4, *bottom left panels*). To keep the output rate at a similar level the rate and strength ($\bar{g}_{exc}$) of the driving input had to be increased. The combined effect results in a shorter dead time and a wider interspike interval histogram. Thus the introduction of the AHP channels, which act to lower the output rate, and the increase in the input rate, which acts to increase the output rate, do not cancel each other (as discussed further in *Modeling different unit types*).

TABLE 2. *Morphological and innervation conditions for the simulations*

| Figure | Input Characteristics | | | $\bar{g}_{AHP}$, mS/cm$^2$ | Comment |
|---|---|---|---|---|---|
| | $L$ | $A_{ss}$ | $A_{tr}$ | | |
| 3 | 0.5 | 1,500 | 1,500 | 0 | Prototype<br>No $Ca^{2+}$<br>$\bar{g}_{exc}$: 2.5 $\mu$S/cm$^2$ |
| 4 and 5 | 0.5 | 3,750 | 2,000 | 26 | Fast chopperlike |
| 7 | 0.5 | 2,000 | 1,000 | 35 | Slow chopperlike |
| 8 | 0.5 | 2,500 | 2,500 | 15 | Bimodal-like<br>Dendritic diam: 4.3 $\mu$m<br>$R_m$: 1,500 $\Omega$/cm$^2$ |
| 9 and 10 | | | | 55 | Slow chopper excitatory series |
| *a* | 0.5 | 1,250 | 1,250 | | |
| *b* | 0.5 | 2,000 | 2,000 | | |
| *c* | 0.5 | 3,000 | 3,000 | | |
| 11 and 12 | 0.5 | 3,000 | 3,000 | 26 | Fast chopper excitatory series |
| *a* | | | | | No additional excitation |
| *b* | 0.3 | 4,000 | 0 | | Additional excitation: 2-ms delay |
| *c* | 0.3 | 6,000 | 0 | | Additional excitation: 2-ms delay |
| 13 and 14 | 0.5 | 6,000 | 2,000 | 26 | Fast chopper inhibitory series |
| | 0.2 | 4,000 | 4,000 | | Additional excitation: 2-ms delay |
| *a* | | | | | No inhibition |
| *b* | Soma | 750 | 0 | | Somatic inhibition: 1-ms delay |
| *c* | Soma | 2,750 | 2,750 | | Somatic inhibition: 1-ms delay |

The time course of the submembrane calcium concentration $[Ca^{2+}]$, and the corresponding time course of the conductance of the calcium-dependent potassium channels $g_{AHP}$, are shown in Fig. 5 along with the spikes generated by the model in response to a simulated input spike train. Both the

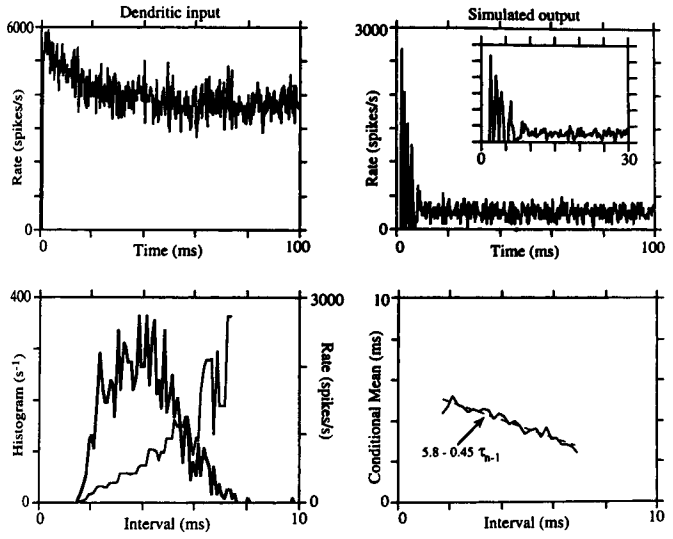


FIG. 4. Final model: fast-chopper–like response characteristics. The final model (Fig. 2), with the reference set of parameters (Table 1), is excited by spike trains produced by an inhomogeneous Poisson process ($A_{ss}$ = 3,750 spikes/s and $A_{tr}$ = 2,000 spikes/s). PST histograms of the input and output spike trains are shown in the *top panels* (binwidth 250 $\mu$s). The initial response of the model includes multiple narrow and closely spaced peaks as typical for the response of fast choppers. The interval histogram and recovery function (*bottom left*, binwidth 100 $\mu$s) are characteristic of slowly driven fast choppers. The best linear fit is superimposed on the conditional mean function (*bottom right*, binwidth 200 $\mu$s) demonstrating negative serial dependence. Compare with Fig. 1, *middle row*. We did not delay the dendritic input to account for latencies that occur along the excitatory input path. Consequently, simulated responses have less latency than do measured responses: an irrelevant discrepancy for our purposes.

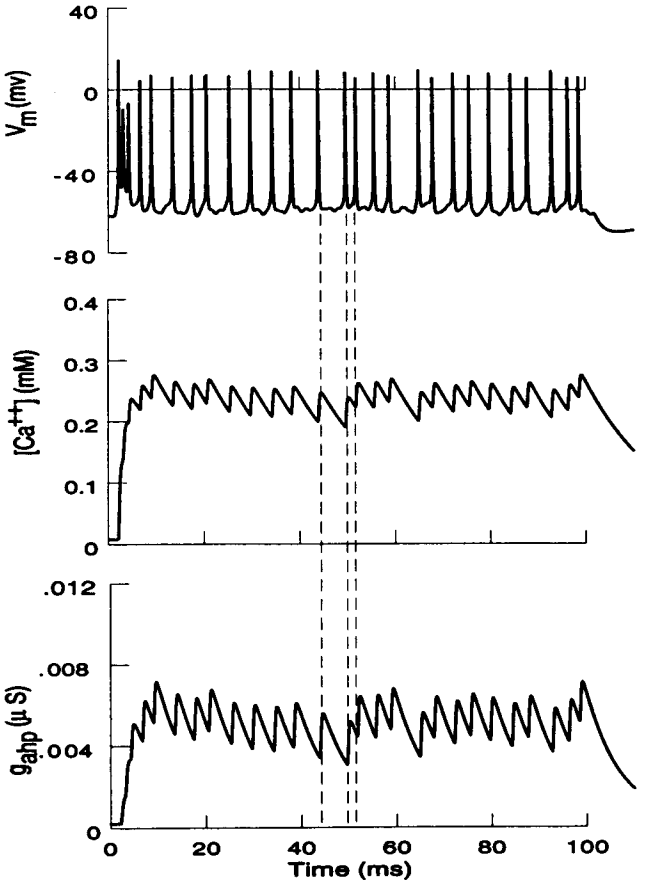


FIG. 5. Calcium dynamics affect serial dependence. The membrane voltage ($V_m$, *top*), submembrane calcium concentration ($\chi$, *middle*), and the conductance of the calcium-dependent potassium channels ($g_{AHP}$, *bottom*) during a simulated tone-burst response of the final model (conditions as in Fig. 4). The initial $Ca^{2+}$ concentration equaled its equilibrium value $\chi_0$. Negative serial dependence is evident in the spike train, and its origin can be traced to the dynamics of $g_{AHP}$ and $\chi$ (note the 3 spike times indicated by the dashed lines).

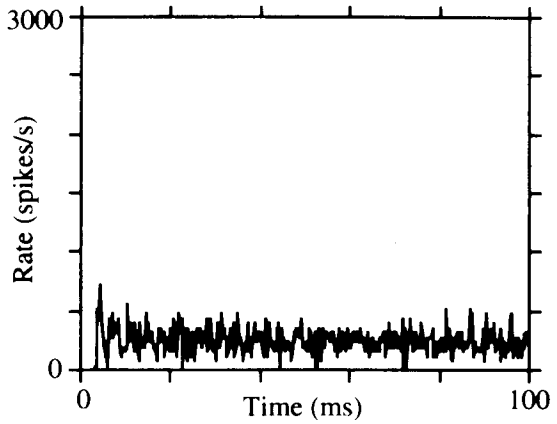


FIG. 6. Effect of initial submembrane calcium concentration. The final model (Fig. 2) with the reference set of parameters is excited as in Fig. 4, except that the initial level of submembrane calcium concentration is forced to the average level reached during the simulated tone-burst response (0.25 mM, see Fig. 5, *middle panel*). The PST histogram of the output spike train (binwidth 250 $\mu$s) lacks the initial chopping response.

submembrane $[Ca^{2+}]$ and $g_{AHP}$ change abruptly in response to stimulus onset and reach new average levels with superimposed spike-triggered dynamics. The occurrence of a spike triggers an abrupt influx of calcium that is followed by a gradual decay of the submembrane $[Ca^{2+}]$, as shown in the *middle panel* of Fig. 5. The time course of $g_{AHP}$ follows closely the time course of submembrane $[Ca^{2+}]$, as shown in the *bottom panel* of Fig. 5. Long intervals provide more time for submembrane $[Ca^{2+}]$ to decay and thus to reach lower levels. Consequently, the level of submembrane $[Ca^{2+}]$ at the beginning of an interval that follows a long interval tends to be low with a corresponding small value for $g_{AHP}$. Because potassium conductance has a shunting effect, the probability of spike initiation increases with smaller values of $g_{AHP}$. Thus serial dependence is mediated by the effect of the interval duration on submembrane $[Ca^{2+}]$, the effect of submembrane $[Ca^{2+}]$ on $g_{AHP}$, and the effect of $g_{AHP}$ on membrane potential and spike initiation.

### *Chopping response results from transient in submembrane* $[Ca^{2+}]$

The time course of the envelope of the transient chopping response resembles the time course of the transient in submembrane calcium concentration $\chi = [Ca^{2+}]$ (Fig. 5, *top* and *middle panels*) rather than the time course of the short-term adaptation in the input rate (Fig. 4, *top left panel*). Indeed, the transient chopping response is not apparent in simulated discharges that are elicited by the model when the initial level of submembrane calcium concentration is forced to the sustained level, as shown in the PST histogram in Fig. 6 (compare with the PST in Fig. 4, *top right panel*). In this case, the lack of a transient in submembrane calcium concentration, and the lack of a corresponding transient in the potassium conductance $g_{AHP}$ results in a response with a negligible transient, even though the driving input is the same as used in generating the response shown in Fig. 4.

### *Modeling different unit types*

The simulated response shown in Fig. 4 exhibits the response characteristics of slowly driven fast choppers (compare with Fig. 1, *middle row*). In particular the initial chopping pattern includes multiple narrow and closely spaced peaks, and the sustained rate is high. The interval histogram and recovery function are characteristic of slowly driven fast choppers in that they do not exhibit the rebound effect at the end of the dead time. It will be shown later (Figs. 12 and 14) that the rebound effect is evoked by this model in response to higher input levels.

Here we concentrate on the minimal set of changes in the model's parameters that are needed in order to elicit responses that are typical of slow choppers and bimodal units. We took the set of parameters used in generating the response analyzed in Fig. 4 as a reference set (Table 1). Slow-chopper–like response patterns can be generated by varying only $\bar{g}_{AHP}$, the maximum conductance level of the calcium-dependent potassium channels (from 26 to 35 mS/cm$^2$), as demonstrated in Fig. 7. The rate of the driving input, shown in the *top left panel* of Fig. 7, is lower than that used to drive the response shown in Fig. 4, but has a similar transient to sustained discharge rate ratio. Typical of slow chopper's tone-burst responses, the initial chopping pattern of the simulated response includes two narrow peaks followed by wider peaks, and the sustained rate is low.

Note that both decreasing the rate of the driving input and increasing $\bar{g}_{AHP}$ have the effect of decreasing the output rate. However, these two parameters affect the output rate through different mechanisms and have distinguishably different effects on the recovery function. Decreasing the input rate has the effect of shifting the recovery function to higher intervals and scaling (rotating) the recovery function downward (clockwise). This is in agreement with the point process

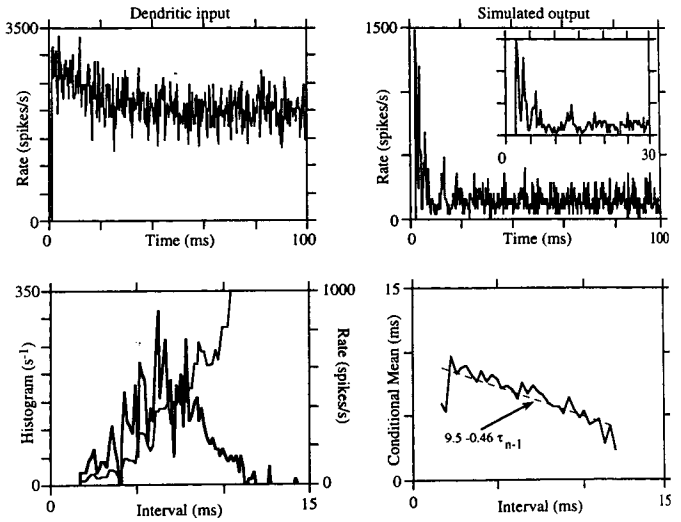


FIG. 7. Final model: slow-chopper–like response characteristics. The final model (Fig. 2), with the reference set of parameters (Table 1, except for the maximum conductance of the AHP channel $\bar{g}_{AHP}$ that is increased to 35 mS/cm$^2$), is excited by spike trains produced by an inhomogeneous Poisson process ($A_{ss}$ = 2,000 spikes/s and $A_{tr}$ = 1,000 spikes/s). The PST histograms of the input and output spike trains are shown in the *top panels* (binwidth 250 $\mu$s). The initial response of the model includes 2 narrow peaks followed by wider peaks, which typifies the slow-chopper-response pattern. The interval histogram and recovery function (*bottom left,* binwidth 150 $\mu$s) are also characteristic of slow choppers. The best linear fit is superimposed on the conditional mean function (*bottom right,* binwidth 300 $\mu$s), thus demonstrating negative serial interspike interval dependence. Compare with Fig. 1, *top row.*

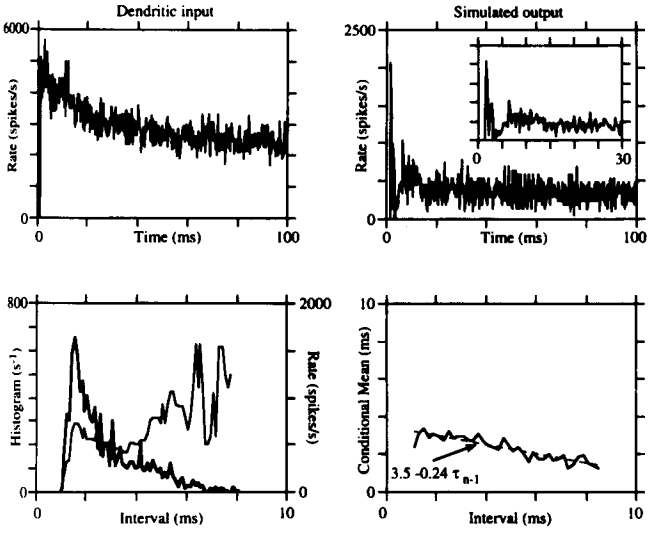


FIG. 8. Final model: bimodal-like response characteristics. The final model (Fig. 2), with a set of parameters modified from those given in Table 1, is excited by spike trains produced by an inhomogeneous Poisson process ($A_{ss} = A_{tr}$ = 2,500 spikes/s). Modifications of the reference set of parameters include *1*) dendritic diameter increased to 4.3 $\mu$m, *2*) dendrite membrane resistance $R_m$ reduced to 1,500 $\Omega/cm^2$, and *3*) maximum conductance of the AHP channels $\bar{g}_{AHP}$ reduced to 15 mS/cm$^2$. The PST histograms of the input and output spike trains are shown in the *top panels* (binwidth 250 $\mu$s). The initial response includes 2 peaks followed by a pause as typical for the response of bimodal neurons. The interval histogram and recovery function (*bottom left,* binwidth 100 $\mu$s) are also characteristic of bimodal neurons. The best linear fit is superimposed on the conditional mean function (*bottom right,* binwidth 200 $\mu$s) demonstrating negative serial dependence. Compare with Fig. 1, *bottom row.*

model of the effect of excitatory stimulus level (Zacksenhouse et al. 1993). In contrast, the conductance of the calcium-dependent potassium channels have a shunting effect similar to the effect of the inhibitory stimulus level. Thus increasing $\bar{g}_{AHP}$ affects only the scaling, but not the origin of the recovery function. Given these differences, decreasing the input rate is not equivalent to increasing the $\bar{g}_{AHP}$. In particular, if the output rate of the model of the fast chopper is reduced by decreasing only the input rate, the resulting recovery function would be too steep and its dead time too long compared with recovery functions of discharges from LSO slow choppers. That input rate is not the only difference between slow and fast choppers is also evident when comparing the transient chopping responses. Discharges from LSO neurons demonstrate that even when a fast chopper and a slow chopper respond at the same output rate, the transient responses differ; the transient response of the fast chopper last longer and include more peaks (cf. Fig. 1*c* and Fig. 2*a* in Zacksenhouse et al. 1993). As was discussed in the context of Fig. 5, the transient response results from a transient in submembrane calcium concentration and not the transient in the input rate. Thus the differences in the transient responses produced by slow and fast choppers have to be related to a difference in one of the calcium-related parameters.

Simulating the responses of bimodal units requires changing additional parameters: *1*) $\bar{g}_{AHP}$ is lowered to 15 mS/cm$^2$, *2*) the dendrites are made thicker (dendritic diameter increased from 3.4 to 4.3 $\mu$m), and *3*) membrane resistance is lowered (from 3,000 to 1,500 $\Omega/cm^2$). The statistical measures of the resulting simulated discharges are shown in Fig. 8 (cf. with Fig. 1, *bottom row*). The interval histogram is typical of bimodal units having a large narrow first mode followed by a smaller and wider second mode that is usually obscured in the first mode's tail. The recovery function exhibits a sequence of distinctive variations characteristic of bimodal units: an abrupt change in discharge rate just after the dead time (the rebound effect), a negative aging section when the recovery function decreases, and a subsequent positive aging section when rate again increases.

### *Modeling the effect of excitatory stimulus level*

The effect of excitatory stimulus level is simulated by varying the rate and innervation of the input, as demonstrated in Figs. 9–12. Increasing the excitatory stimulus level results in a corresponding increase in the rate of incoming EPSPs. This effect is modeled by either increasing the input rate at the same synaptic locations along the dendritic branches or by inducing new synapses located closer to the soma.

The effects of excitatory stimulus level on the measured characteristics of a slow chopper are shown in Figs. 9 and 10, right column. By increasing $\bar{g}_{AHP}$ to 55 mS/cm$^2$ and adjusting the input rate, the model can be tailored to simulate closely the response of this particular slow chopper to the lowest stimulus level (Figs. 9 and 10, *top panels*). The responses to the higher stimulus levels are simulated by

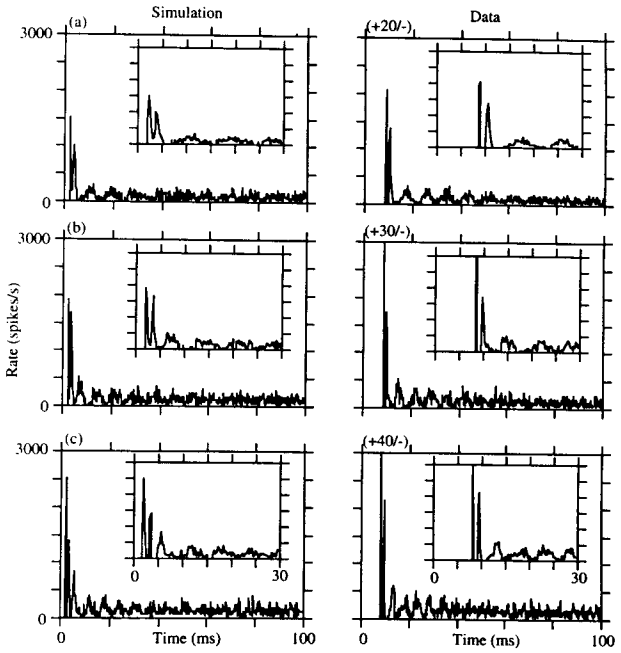


FIG. 9. Excitatory series: slow chopper, PST histograms. PST histograms (binwidth 250 $\mu$s) of measured tone-burst responses to increasing excitatory stimulus levels [*right column;* slow chopper A in Zacksenhouse et al. (1995)] are compared with PST histograms of simulated responses (*left column*) generated by exciting a single instance of the model with input processes having increasing rates. The stimulus levels, expressed in dB above the unit threshold (ipsilateral level/contralateral level), are indicated above the *top left corner* of the measured histograms. The final model with the reference set of parameters (Table 1 except for the maximum conductance of the AHP channel $\bar{g}_{AHP}$ that is set to 55 mS/cm$^2$) is excited by spike trains produced by 3 different inhomogeneous Poisson processes: *a*, $A_{ss} = A_{tr}$ = 1,250 spikes/s; *b*, $A_{ss} = A_{tr}$ = 2,000 spikes/s; and *c*, $A_{ss} = A_{tr}$ = 3,000 spikes/s.

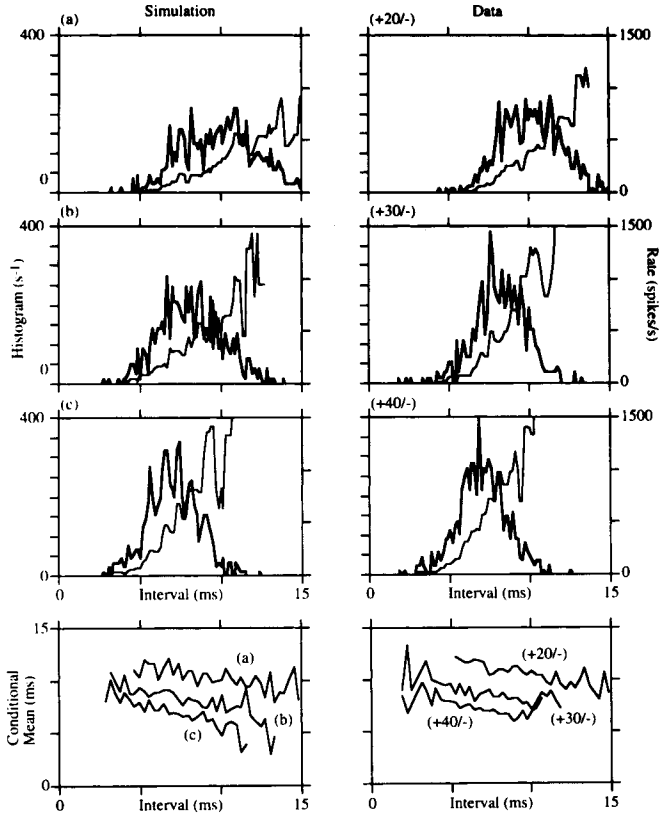


FIG. 10. Excitatory series: slow-chopper interval statistics. Interval statistics, derived from the measured and simulated responses described in Fig. 9, are compared. Interval histograms (thin lines, binwidth 150 $\mu$s), and recovery functions (bold lines) are shown in the *top 3 panels,* whereas conditional mean functions are shown in the *bottom panels* (binwidth 300 $\mu$s).

increasing the input rate at the same location (at the middle of each dendritic branch; Figs. 9 and 10, *bottom panels*). The measured as well as the simulated responses are characterized by two narrow peaks followed by wider peaks in PST histograms. In both cases, the input rate affects *1*) the sustained rate, *2*) the amplitude of the narrow peaks, and *3*) the spacing of the wide peaks. The interval histograms, derived from either measured or simulated responses, remain approximately symmetric under all conditions. The conditional mean functions are parallel, indicating the invariance of serial dependence on discharge rate.

The effects of excitatory stimulus level on the measured characteristics of a fast chopper are shown in Figs. 11 and 12, *right column.* By adjusting the input rate, the model with the reference set of parameters closely simulates the response of this fast chopper to the lowest stimulus level (Figs. 11 and 12, *top panels*). The responses to the higher stimulus levels are simulated by evoking additional synapses closer to the soma ($L$ = 0.3) with a 2-ms delay (Figs. 11 and 12, *bottom panels*). The measured as well as the simulated responses are characterized by multiple narrow and closely spaced peaks in the PST histograms. In both cases, the input rate affects the sustained rate and the extent of the chopping response. The interval histograms, derived from either measured or simulated responses, become more skewed as the input rate increases. The postspike discharge rate, characterizing the measured or simulated discharges, increases abruptly at the end of the dead time, as is apparent in the corresponding recovery functions.

### *Modeling binaural interaction*

Our previous work on point process modeling of LSO binaural discharges suggests that the inhibition exhibited by LSO neurons is mainly a shunting effect (inhibition increases conductance, thereby shunting membrane current). This shunting effect is best mediated by inhibitory synapses located close to the soma that are capable of producing large conductance changes (Blomfield 1974). The morphology of LSO neurons indicates that the inhibitory synapses are located on the somatic compartment. Based on intracellular measurements of EPSPs and IPSPs in LSO neurons in the gerbil (Sanes 1990), the IPSPs are twice as long as the EPSPs. To obtain that effect despite the relative locations of the excitatory and inhibitory synapses, the time constant of the inhibitory synapses is increased fivefold (Table 1), with the desired increase in the overall inhibitory conductance change.

The effects of inhibitory stimulus level on the measured characteristics of a fast chopper are shown in Figs. 13 and 14, *right column.* The model used to simulate these responses is the same one used in simulating the response shown in

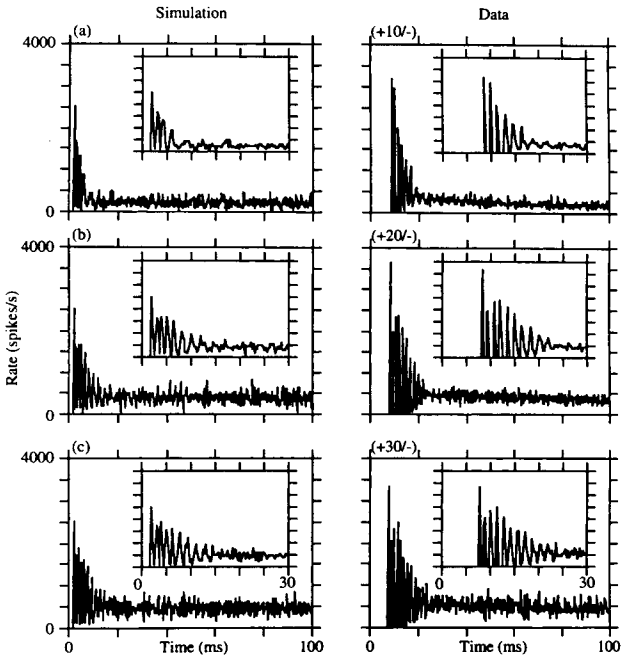


FIG. 11. Excitatory series: fast chopper, PST histograms. PST histograms (binwidth 250 $\mu$s) of measured tone-burst responses to increasing excitatory stimulus levels [*right column;* fast chopper A in Zacksenhouse et al. (1995)] are compared with PST histograms of simulated responses (*left column*) generated by exciting a single instance of the model with input processes having increasing rates. The stimulus levels, expressed in dB above the unit threshold (ipsilateral level/contralateral level), are indicated above the *top left corner* of the measured histograms. The final model with the reference set of parameters is excited at the middle of each dendritic branch by spike trains produced by inhomogeneous Poisson process ($A_{ss}$ = $A_{tr}$ = 3,000 spikes/s). Additional synapses are introduced at $L$ = 0.3 and excited, after a 2-ms delay, by spike trains produced by different homogeneous Poisson processes: *a,* none; *b,* $A_{ss}$ = 4,000 spikes/s; and *c,* $A_{ss}$ = 6,000 spikes/s.

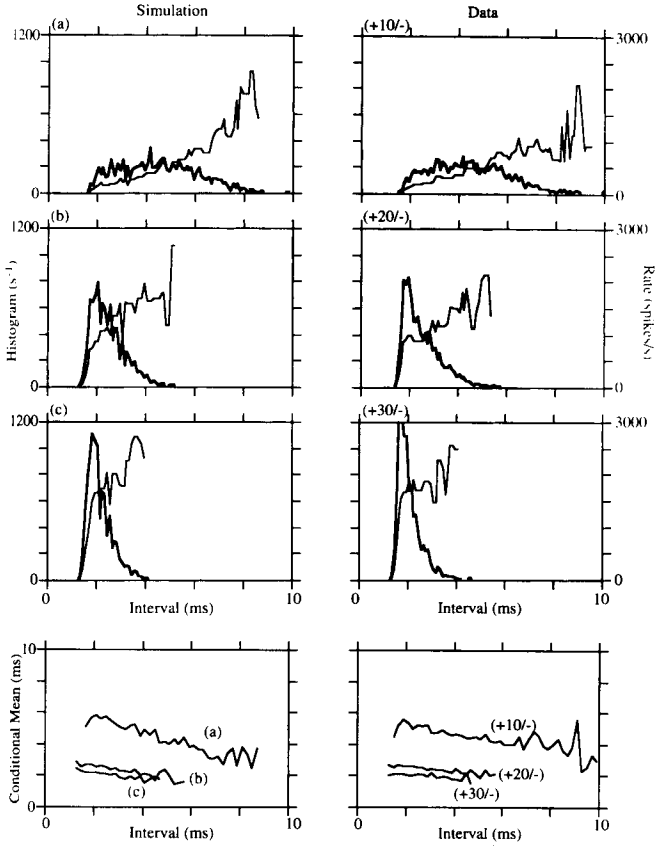


FIG. 12. Excitatory series: fast-chopper interval statistics. Interval statistics, derived from the measured and simulated responses described in Fig. 11, are compared. Interval histograms (thin lines, binwidth 100 $\mu$s), and recovery functions (bold lines) are shown in the *top 3 panels,* whereas conditional mean functions are shown in the *bottom panels* (binwidth 200 $\mu$s).

Fig. 4 (and those shown in Figs. 11 and 12, simulating another fast chopper) with different inputs. The high excitatory stimulus level is modeled by increasing the input rate at the synapses located at the middle of the dendritic branches and by evoking new excitatory synapses closer to the soma ($L = 0.2$) with a 2-ms delay. The simulated excitatory response (*top left panels*) is typical of fast choppers: the chopping response includes multiple narrow and closely spaced peaks, and the postspike discharge rate changes abruptly at the end of the dead time (as evident in the recovery function). Inhibition, at increasing rates, affects both the measured and simulated binaural responses in a similar way: the output rate decreases, the duration of the chopping response shortens, and the interval histograms becomes more skewed, while the conditional mean functions remain relatively parallel.

Although the duration and timing of the chopping responses are simulated well, the peaks are not as high as those derived from measured responses. This discrepancy may be attributed to the loss of synchronization that may be present in the real input but is lacking in our simplified superposition model (see the section on input characteristics).

## DISCUSSION

We have presented a compartmental model of LSO neurons that successfully produces spike trains having the distinctive characteristics of measured LSO neuron discharges. The model is based on intracellular measurements and on insights gained from analysis and modeling of recorded spike trains. The modeling success supports our hypotheses concerning the biophysical origin of serial dependence and the nature of inhibitory processes in LSO neurons.

We have shown that the negative serial dependence exhibited by LSO neuron discharges cannot be produced by neurons having only classic Hodgkin-Huxley $Na^+$ and $K^+$ channels. Calcium and calcium-dependent potassium channels have been shown to generate negative serial dependence of the nature observed in LSO neuron discharges. In particular, the strength of serial dependence, measured by the slope of the conditional mean function, is independent of the stimulus conditions in both measured and simulated discharges (Figs. 10, 12, and 14). Furthermore, the transient change in calcium concentration at the onset of a tone-burst response has been shown to induce the distinctive transient chopping response. Thus both the serial dependence and the chopping response can emerge from calcium-dependent mechanisms. Further support of the role of calcium mechanisms in the activity of LSO neurons requires calcium imaging experiments to validate the existence of calcium channels in LSO cell membrane.

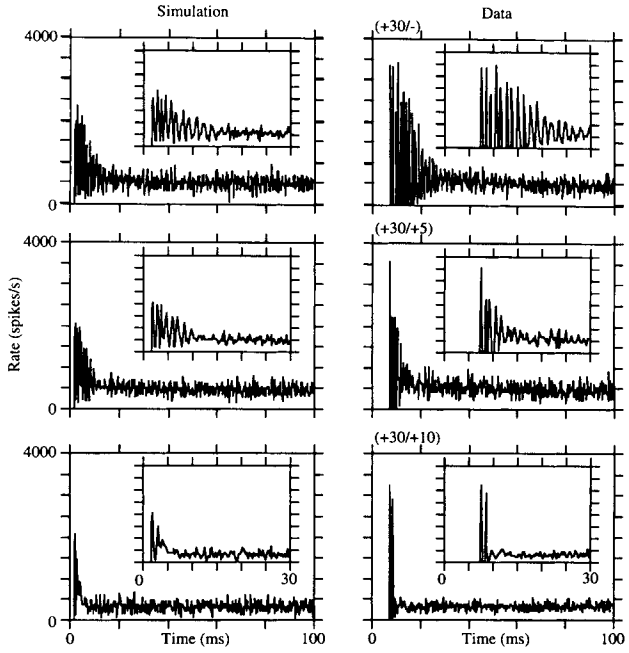


FIG. 13. Inhibitory series: fast chopper, PST histograms. PST histograms (binwidth 250 $\mu$s) of measured tone-burst responses to different binaural stimuli [*right column;* fast chopper B in Zacksenhouse et al. (1995)] are compared with PST histograms of simulated responses (*left column*) generated by exciting a single instance of the model with the same input processes and inhibiting it with input processes having increasing rates. The stimulus levels, expressed in dB above the unit threshold (ipsilateral level/contralateral level), are indicated above the *top left corner* of the measured histograms. The final model with the reference set of parameters is excited at the middle of each dendritic branch by spike trains produced by inhomogeneous Poisson process ($A_{ss}$ = 6,000 spikes/s and $A_{tr}$ = 2,000 spikes/s), and at $L = 0.2$ along each dendritic branch by spike trains produced by a different inhomogeneous Poisson process ($A_{ss} = A_{tr}$ = 4,000 spikes/s), and delayed by 2 ms. Inhibitory synapses are added in the soma and excited, after a 1-ms delay, by spike trains produced by different inhomogeneous Poisson processes: *a,* none; *b,* $A_{ss}$ = 750 spikes/s; and *c,* $A_{ss} = A_{tr}$ = 2,750 spikes/s.

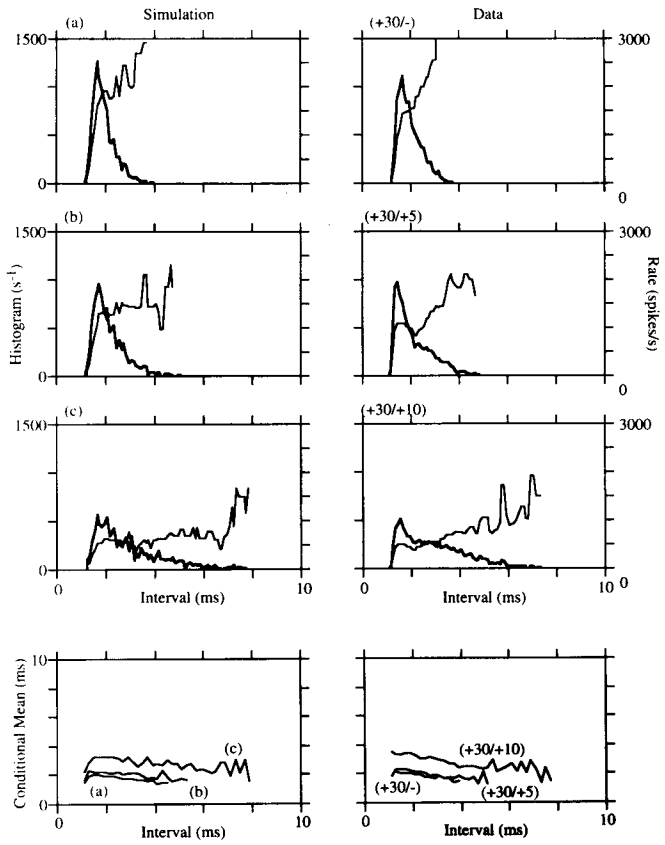


FIG. 14. Inhibitory series: fast-chopper interval statistics. Interval statistics, derived from the measured and simulated responses described in Fig. 13, are compared. Interval histograms (thin lines, binwidth 100 $\mu$s), and recovery functions (bold lines) are shown in the *top 3 panels,* whereas conditional mean functions are shown in the *bottom panels* (binwidth 200 $\mu$s).

It was shown previously that the inhibitory process in LSO neurons is not equivalent to reduced excitation. Point process analyses and modeling suggested that shunting inhibition dominates the inhibitory process. Morphological, pharmacological, and intracellular measurements all support this conclusion, indicating that inhibitory synapses are proximal or somatic, are mediated by chloride channels, and produce long-lasting conductance changes. Our model demonstrates that indeed such inhibitory processes produce the observed inhibitory response patterns and hence are not equivalent to cancellation of excitatory processes. Thus the model suggests a correspondence between the characteristics of measured spike trains and underlying biophysical membrane characteristics.

By changing the maximum conductance of the AHP channel, the model is successful in reproducing the tone-burst responses of different slow and fast choppers. Changes in the maximum conductance of a channel reflects changes in the density of the corresponding channel. Thus the modeling work suggests that one of the major differences between slow and fast choppers is the density of the calcium-dependent potassium channels. In addition, slow and fast choppers seem to differ in the input innervation; simulations of the responses of fast choppers require higher total input rates. Model bimodal units differ also in the passive characteristics of their dendrites, having thicker dendrites with a more conductive membrane.

The passive properties of the model are based on the membrane characteristics of LSO neurons in the mouse and gerbil. Characterization of the corresponding physiological properties of LSO neurons in the cat would be beneficial in fine tuning the model. The active properties of the model are similar in general to those used in compartmental models of AVCN neurons (Banks and Sachs 1991) ($Na^+$ and $K^+$ channels) and CA3 hippocampal neurons (Traub et al. 1991) (calcium mechanisms). However, some parameter values had to be changed significantly to produce spike trains characteristic of LSO discharges. The differences among the models' active channels are indicative of the roles of these channels in the different structures. Thus the success of these models suggests that the same channels can be tuned to produce spike trains with different characteristics and to carry different types of computations. Voltage-clamp experiments in LSO neurons (preferably in the cat) would be beneficial in evaluating this conclusion.

The compartmental model presented here predicts the input-output relation governing the responses of LSO neurons. Coupled with models of the inputs to the LSO, the model can predict the response of LSO neurons to novel stimuli and thus to facilitate studies of the role of LSO in signal localization and enhancement. Furthermore, this single neuron model may be extended to a complete model of the LSO network. Compartmental models of the AVCN spherical/bushy cells, AVCN globular/bushy cells, and MNTB principal/globular cells are needed to simulate the spike trains that feed into the model of the LSO neurons.

## APPENDIX

We use the NEURON program to develop the model. The anatomic, electronic, and membrane parameters are listed in Table 1.

The default passive membrane mechanism is inserted in the dendritic membrane. The active mechanisms, inserted in the axonal and somatic membranes, are detailed here. The somatic membrane includes four types of active channels: $Na^+$, $K^+$, $Ca^{2+}$, and AHP (calcium-dependent potassium channels that produce the afterhyperpolarization), whereas the axonal membrane includes only $Na^+$ and $K^+$ channels. The current densities through each of these channels ($i_{channel}$ in mA/cm$^2$) are

$$i_{Na} = \bar{g}_{Na} m^3 h (V - E_{Na})$$

$$i_K = \bar{g}_K n^4 (V - E_K)$$

$$i_{Ca} = \bar{g}_{Ca} s^5 r (V - E_{Ca})$$

$$i_{AHP} = \bar{g}_{AHP} q (V - E_K)$$

where $\bar{g}_{channel}$ is the maximum conductance per unit area, $E_{channel}$ is the reversal potential, $m$, $n$, $s$, and $q$ are the activation state variables, and $h$ and $r$ are the inactivation state variables. The state variables obey the Hodgkin-Huxley–like first-order differential equations given for example by

$$\frac{dm}{dt} = T_{fac}[\alpha_m (1 - m) - \beta_m m]$$

where $\alpha$ and $\beta$ are the rate functions and $T_{fac}$ accounts for the rate parameters' temperature dependence ($T_{fac} = 16$) (Banks and Sachs 1991). The rate functions of the state variables $m$, $h$, $n$, and $s$ depend on the voltage $V$, whereas the rate functions of the state

TABLE A1. *Rate functions of the activation and inactivation state variables of active channels in the somatic and axonal compartments*

Sodium activation

$$\alpha_m = -0.1 \frac{V + 37 + M_{sh}}{\exp[-(V + 37 + M_{sh})/10] - 1}$$

$$\beta_m = 4 \exp[-(V + 62 + M_{sh})/18]$$

$$M_{sh} = 2.3 \text{ mV}$$

Sodium inactivation

$$\alpha_h = 0.07 \exp[-(V + 62 + H_{sh})/20]$$

$$\beta_h = \frac{1}{\exp[-(V + 32 + H_{sh})/10] + 1}$$

$H_{sh}$ (axon) $= -10.8$ mV; $H_{sh}$ (soma) $= -10.0$ mV

Potassium activation

$$\alpha_n = -0.01 \frac{V + 52 + N_{sh}}{\exp[-(V + 52 + N_{sh})/10] - 1}$$

$$\beta_n = 0.125 \exp[-(V + 62 + N_{sh})/80]$$

$N_{sh}$ (axon) $= 2.6$ mV; $N_{sh}$ (soma) $= -1.3$ mV

Calcium activation

$$\alpha_s = -1.2 \frac{V + 2}{\exp[-(V + 2)/12.5] - 1}$$

$$\beta_s = 0.045 \frac{V + 17}{\exp[(V + 17)/12.5] - 1}$$

Calcium inactivation

$$\alpha_r = 14.4$$

$$\beta_r = 56 \frac{0.1 - \chi}{\exp[(0.1 - \chi)/0.025] - 1}$$

Calcium-dependent potassium activation

$$\alpha_q = 2925 \frac{0.3 - \chi}{\exp[(0.3 - \chi)/0.05] - 1}$$

$$\beta_q = 300$$

Membrane voltage $V$ is expressed in mV.

variables $r$ and $q$ depend on the submembrane calcium concentration $\chi$, as given in Table A1.

Submembrane calcium concentration, in the outermost shell of depth $d = 315$ Å, is governed by a first-order differential equation

$$\frac{d\chi}{dt} = \frac{-0.001c}{d} i_{Ca} - \frac{\chi - \chi_0}{\tau_p}$$

where $c = 1/(2 * F)$ is a conversion constant ($F = 9.6 \times 10^4$ Coul/mol, Faraday's constant), 0.001 is a conversion constant from $s^{-1}$ to $ms^{-1}$, $\tau_p$ is the time constant of the calcium pump, and $\chi_0$ is the equilibrium concentration for the pump. We do not model the inward diffusion of calcium explicitly. Instead, the above first-order decay equation provides a first-order approximation to the diffusion process while mainly describing the outward pumping of calcium.

The kinetics of the $Na^+$ and $K^+$ channels are governed by equations similar to those used by Banks and Sachs in their model of chopper units in the AVCN (Banks and Sachs 1991). The major difference is that we use a higher value for $\delta_0$ (0.8 instead of 0.19, see the rate functions for $n$ in Table A1), which reduces the effect of the $\delta$ function. With $\delta_0 = 1$, the $\delta$ function has no effect. A lower value increases the time constant of $n$ and slows the kinetics of the $K^+$ channels with the overall effect of reducing the discharge rate.

The kinetics of the $Ca^{2+}$ and the AHP channels are governed by equations similar to those used by Traub for simulating bursting in CA3 hippocampal neurons but with significantly different parameter values. Also, here the AHP channels are voltage independent; their kinetics depend only on calcium. The major effect of using different parameters for the rate functions is that the calcium-dependent state variables $r$ and $q$ vary at lower calcium concentrations. Also, the calcium activation is ~10 times faster (the time constant of the voltage-dependent calcium-activation state variable $s$ is ~10 times smaller) and increases at lower membrane potentials; allowing more calcium to flow in during each spike.

We thank Prof. Hines for support in installing and using NEURON. We thank undergraduate students M. Harms and E. Zertuche, who helped develop earlier versions of the model.

This work was supported by a grant from the Office of Naval Research.

Address for reprint requests: D. Johnson, George R. Brown School of Engineering, Rice University, 6100 Main, 2041 Duncan Hall, Houston, TX 77005-1892.

Received 15 January 1997; accepted in final form 1 March 1998.

REFERENCES

BANKS, M. I. AND SACHS, M. B. Regularity analysis in a compartmental model of chopper units. *J. Neurophysiol.* 65: 606–629, 1991.

BLOMFIELD, S. Arithmetical operations performed by nerve cells. *Brain Res.* 69: 115–124, 1974.

BLUM, J. AND REED, M. Further studies of a model for azimuthal encoding: lateral superior olive neuron response curves and developmental processes. *J. Acoust. Soc. Am.* 90: 1968–1978, 1991.

BOUDREAU, J. C. AND TSUCHITANI, C. Binaural interaction in the superior olive S-segment. *J. Neurophysiol.* 31: 422–454, 1968.

BOUDREAU, J. C. AND TSUCHITANI, C. Cat superior olive S-segment cell discharge to tonal stimuli. In: *Contributions to Sensory Physiology,* edited by W. D. Neff. New York: Academic, 1970, vol. 4, p. 143–213.

BOURK, T. R. *Electrical Responses of Neural Units in the Anteroventral Cochlear Nucleus of the Cat* (PhD thesis). Cambridge, MA: MIT, 1976.

CANT, N. B. The fine structure of the lateral superior olivary nucleus of the cat. *J. Comp. Neurol.* 227: 63–77, 1984.

CANT, N. B. Projections to the lateral and medial superior olivary nuclei from the spherical and globular bushy cells of the anteroventral cochlear nucleus. In: *Neurobiology of Hearing. The Central Auditory System,* edited by R. Altschuler, D. Hoffman, D. Bobbin, and B. Clopton. New York: Raven, 1991, vol. III, p. 99–119.

CANT, N. B. AND CASSEDAY, J. H. Projections from the anteroventral cochlear nucleus to the lateral and medial superior olivary nuclei. *J. Comp. Neurol.* 247: 457–476, 1986.

COLBURN, H. S. AND MOSS, P. J. Binaural interaction models and mechanisms. In: *Neuronal Mechanisms of Hearing,* edited by J. Syka and L. Aitkin. New York: Plenum, 1981, p. 283–288.

DABAK, A. AND JOHNSON, D. H. Function-based modeling of binaural interactions: interaural phase. *Hear. Res.* 58: 200–212, 1992.

GLENDENNING, K. K., HUTSON, K. A., NUDO, R. J., AND MASTERTON, R. B. Acoustic chiasm. II. Anatomical basis of binaurality in lateral superior olive of cat. *J. Comp. Neurol.* 232: 261–285, 1985.

GOLDBERG, J. M. AND BROWN, P. B. Response of binaural neurons of dog superior olivary complex to dichotic tonal stimuli: some physiological mechanisms of sound localization. *J. Neurophysiol.* 32: 613–636, 1969.

GUINAN, J. J., JR., NORRIS, B. E., AND GUINAN, S. S. Single auditory units in the superior olivary complex. II. Locations of unit categories and tonotopic organization. *Int. J. Neurosci.* 4: 147–166, 1972.

HILLE, B. *Ionic Channels of Excitable Membranes* (2nd ed.). Sunderland, MA: Sinauer, 1992.

HODGKIN, A. AND HUXLEY, A. A quantitative description of membrane current and its application to conduction and excitation in nerve. *J. Physiol. (Lond.)* 117: 500–544, 1952.

JOHNSON, D. H. Point process models of single-neuron discharges. *J. Comput. Neurosci.* 3: 275–299, 1996.

JOHNSON, D. H., ZACKSENHOUSE, M., WILLIAMS, J., AND TSUCHITANI, C. Single-neuron modeling constrained by spike train measurements. In: *Computational Neuroscience '94.* Monterey, CA, 1994a.

JOHNSON, D. H. The relationship of post-stimulus time and interval histograms to the timing characteristics of spike trains. *Biophys. J.* 22: 413–430, 1978.

JOHNSON, D. H., TSUCHITANI, C., LINEBARGER, D. A., AND JOHNSON, M. The application of a point process model to the single unit responses of the cat lateral superior olive to ipsilaterally presented tones. *Hear. Res.* 21: 135–159, 1986.

JOHNSON, D. H., WILLIAMS, J., AND TSUCHITANI, C. Computer simulation of single LSO neurons. In: *ARO MidWinter Meeting.* St. Petersburg Beach, FL, 1994b.

MOORE, M. J. AND CASPARY, D. M. Strychnine blocks binaural inhibition in lateral superior olivary neurons. *J. Neurosci.* 3: 237–242, 1983.

PFEIFFER, R. R. Classification of response patterns of spike discharges for units in the cochlear nucleus: Tone-burst stimulation. *Exp. Brain Res.* 1: 220–235, 1966.

RALL, W. Cable theory for dendritic neurons. In: *Methods in Neuron Modeling,* edited by C. Koch and I. Segev. Cambridge, MA: MIT Press, 1989, p. 9–62.

REED, M. AND BLUM, J. A model for the computation and encoding of azimuthal information by the lateral superior olive. *J. Acoust. Soc. Am.* 88: 1442–1453, 1990.

SANES, D. H. An in vitro analysis of sound localization mechanisms in the gerbil lateral superior olive. *J. Neurosci.* 10: 3494–3506, 1990.

SMITH, C. E. AND GOLDBERG, J. M. A stochastic afterhyperpolarization model of repetitive activity in vestibular afferents. *Biol. Cybern.* 54: 41–51, 1986.

SNYDER, D. L. *Random Point Processes.* New York: Wiley, 1975.

TRAUB, R. Simulation of intrinsic bursting in CA3 hippocampal neurons. *Neuroscience* 5: 1233–1242, 1982.

TRAUB, R., WONG, R., MILES, R., AND MICHELSON, H. A model of a CA3 hippocampal pyramidal neurons incorporating voltage-clamp data on intrinsic conductances. *J. Neurophysiol.* 66: 635–650, 1991.

TSUCHITANI, C. Discharge patterns of cat lateral superior olivary units to ipsilateral tone-burst stimuli. *J. Neurophysiol.* 47: 479–500, 1982.

TSUCHITANI, C. The inhibition of cat lateral superior olivary unit excitatory responses to binaural tone bursts. II. The sustained discharges. *J. Neurophysiol.* 59: 184–211, 1988a.

TSUCHITANI, C. The inhibition of cat lateral superior olivary unit excitatory responses to binaural tone bursts. I. The transient chopper discharges. *J. Neurophysiol.* 59: 164–183, 1988b.

TSUCHITANI, C. AND JOHNSON, D. H. The effects of ipsilateral tone-burst stimulus level on the discharge patterns of cat lateral superior olivary units. *J. Acoust. Soc. Am.* 77: 1484–1496, 1985.

WENTHOLD, R. J., HUIE, D., ALTSCHULER, R. A., AND REEKS, K. A. Glycine immunoreactivity localized in the cochlear nucleus and superior olivary complex. *Neuroscience* 22: 897–912, 1987.

WU, S. H. AND KELLY, J. B. Physiological properties of neurons in the mouse superior olive: membrane characteristics and postsynaptic responses studied in vitro. *J. Neurophysiol.* 65: 230–246, 1991.

ZACKSENHOUSE, M. *Point-Process Modeling of Excitatory/Inhibitory Interactions in LSO Neurons* (PhD thesis). Houston, TX: Rice University, 1993.

ZACKSENHOUSE, M., JOHNSON, D. H., AND TSUCHITANI, C. Excitatory/inhibitory interaction in the LSO revealed by point process modeling. *Hear. Res.* 62: 105–123, 1992.

ZACKSENHOUSE, M., JOHNSON, D. H., AND TSUCHITANI, C. Excitation effects on LSO unit sustained responses: point process characterization. *Hear. Res.* 68: 202–216, 1993.

ZACKSENHOUSE, M., JOHNSON, D. H., AND TSUCHITANI, C. Transient effects during the chopping response of LSO neurons. *J. Acoust. Soc. Am.* 98: 1410–1422, 1995.